Applied Science Innovation (ASI)
Published by College of Physical and Applied Sciences, MOUAU

- *Received:* 03 May 2026
- *Revised*: 14 June 2026
- *Accepted:* 25 June 2026
- *Published:* 14 July 2026

METAL OXIDE MODIFICATION OF GROUNDNUT SHELL BIOCHAR FOR ENHANCED REMOVAL OF AMOXICILLIN FROM WATER

Izubundu B. Onyebuenyi[1]*, Nkoli M. Mgbemena,[2], Marc N. Ogbuagu,[3] and Achibong I. Nelson.[4]

[1]**Department of Pure and Industrial Chemistry, University of Calabar, Calabar Nigeria.**
[23]**Department of Chemistry, Michael Okpara University of Agriculture, Umudike Abia State, Nigeria.**
[4]**Department of Chemistry, College of Education, Afaha Nsit, P.M.B. 1091 Etinan, Akwa Ibom State, Nigeria**

***Corresponding author: zubbybrown@gmail.com**

ABSTRACT

The contamination of aquatic environments by antibiotic residues represents a critical global health challenge, necessitating the development of efficient and low-cost removal technologies. This study reports the synthesis, physicochemical characterization, and amoxicillin (AMX) adsorption performance of groundnut shell biochar (GSB) and copper oxide-doped GSB (CuO@GSB) as sustainable adsorbents for aqueous-phase antibiotic remediation. GSB was produced by pyrolysis of groundnut shell biomass, and CuO@GSB was synthesized by wet impregnation with a copper precursor salt followed by calcination. Both materials were characterized using Fourier-Transform Infrared (FT-IR) spectroscopy, X-ray diffraction (XRD) with Rietveld refinement, Brunauer-Emmett-Teller (BET) surface area and porosity analysis, energy dispersive X-ray spectroscopy (EDX), and scanning electron microscopy (SEM). FT-IR confirmed the introduction of Cu-OH surface species and Si-O-Cu lattice vibrations in CuO@GSB, alongside the loss of the carboxyl carbonyl band (1735 cm^{-1}) present in pristine GSB. XRD identified Chalcanthite ($CuSO_4 \cdot 5H_2O$) as the principal copper phase in CuO@GSB, with Quartz and Mullite retained in both materials. BET analysis revealed that CuO loading increased the surface area from 206.7 m^2/g (GSB) to 288.5 m^2/g (CuO@GSB), with both materials classified as mesoporous (pore diameter ~2.1 nm). EDX confirmed copper incorporation at 19.72 at % in CuO@GSB, while SEM revealed a biphasic CuO nanoparticle coating on the biochar scaffold. Adsorption isotherms fitted the Sips and Temkin models most accurately ($R^2 \approx 0.98$-0.99), indicating heterogeneous surface adsorption. CuO@GSB outperformed pristine GSB for AMX removal, achieving a Langmuir maximum adsorption capacity of 9.59 mg g^{-1} versus 6.91 mg g^{-1}, attributed to enhanced Lewis acid coordination and electrostatic interactions introduced by CuO surface sites. These findings demonstrate the potential of agricultural waste-derived metal oxide biochar composites as effective adsorbents for antibiotic pollutant removal from water.

Keywords: Groundnut shell biochar, Copper oxide, Amoxicillin, Adsorption, Water remediation.

1. Introduction

The widespread occurrence of antibiotic residues in aquatic environments has emerged as one of the most pressing environmental health concerns of the 21st century. The global consumption of antibiotics continues to escalate, driven by expanding human healthcare needs, intensive livestock farming, and aquaculture

(Klein et al., 2024). A substantial fraction of these pharmaceuticals is excreted in biologically active forms and enters surface water, groundwater, and effluent streams through municipal wastewater treatment plants (WWTPs), agricultural runoff, and pharmaceutical manufacturing discharge (GBD AMR Collaborators, 2024(a)).

Amoxicillin (AMX), a broad-spectrum beta-lactam antibiotic, is among the most prescribed antibiotics globally owing to its effectiveness against both Gram-positive and Gram-negative bacterial infections and its relatively low cost. Its wide therapeutic application has led to its frequent detection in surface waters, hospital effluents, and receiving water bodies at concentrations ranging from nanograms to micrograms per litre (Adu-Poku et al., 2024). Residual AMX contributes to aquatic ecotoxicity and antimicrobial resistance selection pressure (Gahrouei et al., 2024). The WHO (2024) and UNEP have jointly acknowledged that antibiotic pollution from pharmaceutical manufacturing and clinical use represents a key driver of AMR propagation in the environment, which is now projected to cause up to 10 million deaths annually by 2050 if left unchecked (GBD AMR Collaborators, 2024(b)).

Conventional water treatment technologies, including biological oxidation, chlorination, coagulation-flocculation, and membrane filtration, have demonstrated limited efficacy in completely removing antibiotic micropollutants owing to their structural stability, polar character, and resistance to biodegradation. Advanced oxidation processes (AOPs) such as UV/H_2O_2 and ozonation can effectively degrade AMX, but their high energy demands and potential for toxic by-product formation preclude broad-scale application in resource-limited settings (Gahrouei et al., 2024). Adsorption, by contrast, offers operational simplicity, cost-effectiveness, regenerability, and absence of secondary pollution, making it the preferred strategy for antibiotic removal at scale.

Biochar has attracted growing interest as a low-cost adsorbent for emerging contaminants in water (Tripathi et al., 2024). Its adsorption performance arises from high surface area, hierarchical porosity, and abundant surface functional groups (Tripathi et al., 2024). Agricultural waste-derived biochars are particularly attractive in resource–limited economies such as Nigeria, where groundnut (*Arachis hypogaea*) is one of the most widely grown crops, generating substantial quantities of shell biomass as agro-industrial residue (FAO, 2024). Conversion of groundnut shells into biochar simultaneously addresses solid waste management and provides a low-cost functional material for environmental remediation. Groundnut shell has previously been valorised both as an unmodified biochar for heavy metal biosorption (Duwiejuah et al., 2018) and, following chemical activation with agents such as KOH, H_3PO_4, and $ZnCl_2$, as a high-surface-area activated carbon (up to ~692 $m^2\ g^{-1}$) for organic pollutant removal (Kumari et al., 2022); related peanut-husk-derived activated carbons have also achieved high tetracycline and amoxicillin adsorption capacities following surfactant functionalisation (Egbedina et al., 2023), underscoring the strong pollutant-removal potential of this feedstock class when combined with activation or surface modification strategies.

Despite the inherent adsorption capacity of unmodified biochars, their performance for specific contaminants can be limited by relatively modest surface areas and restricted active site densities. Metal oxide doping–particularly with transition metal oxides such as CuO, ZnO, MgO, and Fe_2O_3 (Brown et al., 2023) – enhances biochar performance by introducing Lewis acid sites, expanding surface area, and generating redox-active centres (Yang et al., 2025). Among these modifiers, copper oxide (CuO) is of particular interest because it provides strong Lewis acidity, is inexpensive and widely available, and its nanoparticulate form offers high surface-to-volume ratios (Frontiers in Bioengineering and Biotechnology, 2025).

Previous investigations have established the utility of metal oxide-modified biochars for removing tetracyclines, fluoroquinolones, and sulfonamides from water, yet studies on beta-lactam antibiotics, and amoxicillin in particular, remain comparatively sparse. Furthermore, the use of groundnut shell as a biochar precursor for metal oxide composite synthesis, and systematic comparison of pristine versus CuO-modified performance for AMX removal, has not been thoroughly documented. The present study addresses these gaps by: (i) synthesizing and fully characterizing GSB and CuO@GSB; (ii) conducting batch adsorption experiments under variable pH, contact time, dosage, initial AMX concentration, and temperature; (iii) applying multiple isotherm and kinetic models to elucidate adsorption mechanisms; and (iv) comparing the AMX adsorption performance of GSB and CuO@GSB with reference to the existing literature. While CuO-doped biochars have previously been examined for other antibiotic classes, and groundnut shell has separately been explored as a precursor for both raw biochar and chemically activated carbon (Duwiejuah et al., 2018; Kumari et al., 2022), the specific combination of groundnut-shell-derived biochar, CuO doping, and amoxicillin as target pollutant investigated here has not previously been reported, providing a distinct feedstock-modifier-pollutant system rather than a replication of prior work.

2. Materials and Methods

2.1 Materials

Groundnut shells were obtained from a local market in Aba, Abia State, Nigeria. Copper (II) sulphate pentahydrate ($CuSO_4 \cdot 5H_2O$, ≥98% purity), amoxicillin trihydrate (AMX, analytical grade), hydrochloric acid (HCl), sodium hydroxide (NaOH), and ethanol (95%) were procured from Sigma-Aldrich (South Africa). All solutions were prepared using deionised water (resistivity ≥18.2 MΩ·cm).

2.2 Preparation of Groundnut Shell Biochar (GSB)

Groundnut shells were thoroughly washed with deionised water to remove dust and surface impurities, oven-dried at 105°C for 24 h, and milled to pass a 2-mm sieve. The dried feedstock was pyrolysed in a muffle furnace under nitrogen atmosphere at 500°C (heating rate 10°C min^{-1}) for 2 h, consistent with optimal conditions for mesoporous agricultural waste biochars reported in the literature (Khater et al., 2024). The resulting black solid was cooled to room temperature under continued N_2 flow, washed sequentially with 0.1 M HCl and deionised water to neutrality (pH 6.8-7.2), oven-dried at 60°C for 12 h, and stored in sealed glass vials.

2.3 Synthesis of CuO@GSB Composite

CuO@GSB was prepared by wet impregnation of GSB with an aqueous copper precursor solution. Briefly, 5.0 g of GSB was dispersed in 100 mL of 0.5 M $CuSO_4 \cdot 5H_2O$ solution with continuous stirring (300 rpm) at 60°C for 4 h to ensure uniform copper ion adsorption onto the biochar surface. The slurry was then dried at 80°C overnight, and the dried solid was calcined in a muffle furnace at 400°C for 2 h under ambient atmosphere to decompose the copper salt precursor and form CuO nanoparticles in situ on the biochar scaffold. The calcined composite was cooled, washed with deionised water, and dried at 80°C for use in characterization and adsorption experiments.

2.4 Physicochemical Characterization

FT-IR spectra were recorded in the range 4000-400 cm^{-1} using a PerkinElmer Spectrum 100 spectrometer with attenuated total reflectance (ATR) sampling. Powder XRD patterns were acquired on a Bruker D8 Advance diffractometer (Cu Kα radiation, λ = 1.5406 Å) over 2θ = 10-80° at a scan speed of 2° min^{-1}. Rietveld refinement was performed using TOPAS 6.0 software to quantify phase composition and lattice parameters. BET surface area, pore volume, and pore size distribution (Barrett-Joyner-Halenda, BJH method) were determined from N_2 adsorption-desorption isotherms measured at -196°C on a Micromeritics 3Flex instrument after outgassing at 200°C for 6 h. SEM-EDX analysis was conducted using a Zeiss Sigma 300 field-emission SEM at 15 kV accelerating voltage, equipped with an Oxford Instruments energy-dispersive X-ray detector for elemental mapping.

2.5 Batch Adsorption Experiments

Batch adsorption experiments were carried out in 250 mL Erlenmeyer flasks containing 100 mL AMX solutions of known concentration, to which known masses of adsorbent (GSB or CuO@GSB) were added. Flasks were agitated on an orbital shaker at 150 rpm. The equilibrium AMX concentration was determined by UV-Vis spectrophotometry (λ_{max} = 230 nm). A calibration curve was constructed within the validated linear response range of the instrument for AMX (1-50 mg L^{-1}, R^2 = 0.999); samples originating from the 100-300 mg L^{-1} initial AMX concentration series were serially diluted 5-fold with deionised water prior to measurement, bringing their absorbance readings within the validated linear range, and a dilution factor of 5 was applied to the concentration read from the calibration curve to back-calculate the true equilibrium concentration.

The effects of the following parameters were investigated: solution pH (2–12, adjusted with 0.1 M HCl/NaOH), contact time (30–180 min), adsorbent dosage (0.02-1.2. g L^{-1}), initial AMX concentration (50-300 mg L^{-1}), and temperature (25, 35, 45, 55, 65, 80 °C). All experiments were performed in triplicate and results expressed as mean ± standard deviation. The adsorption capacity at equilibrium (q_e, mg g^{-1}) and percent removal were calculated using Equations (1) and (2):

$$q_e = \frac{(Co-Ce)xv}{m} \quad (1)$$

$$\%\text{Removal} = \frac{(\text{Co}-\text{Ce})}{Co}100 \quad (2)$$

where C_0 and C_e (mg L^{-1}) are the initial and equilibrium AMX concentrations, V (L) the solution volume, and m (g) the adsorbent mass.

2.6 Adsorption Isotherm Models

Equilibrium data were fitted to the two-parameter Langmuir, Freundlich, and Temkin models, and the three-parameter Sips model as expressed in equations iii-vi (Pham et al., 2024; Efficient Removal, 2020):

$$q_e = \frac{q_{\max} K_L C_e}{1+K_L C_e} \quad (3)$$

$$q_e = K_F C_e^{1/n} \quad (4)$$

$$q_e = \frac{RT}{b_T}\ln\left(A_T C_e\right) \quad (5)$$

$$q_e = \frac{\text{qms(KsCe)ms}}{[1 + \text{(KsCe)ms}]} \quad (6)$$

Model fits were evaluated using the coefficient of determination (R^2), chi-square (χ^2), and root mean square error (RMSE).

3. Results and Discussion

3.1 FT-IR Spectroscopy

The FT-IR spectra of GSB and CuO@GSB are presented in Figure 1. The spectrum of GSB exhibited characteristic absorption bands consistent with a carbonaceous lignocellulosic-derived biochar: a broad O-H stretching vibration at ~3400 cm^{-1} associated with surface hydroxyl groups and physisorbed water, a C-H aliphatic stretch at ~2920 cm^{-1}, a C=O carboxyl carbonyl band at 1735 cm^{-1}, C=C aromatic stretching at ~1590 cm^{-1}, C-O stretching at ~1230 cm^{-1}, and Si-O-Si lattice vibrations at ~1050 cm^{-1}, consistent with the silicate mineralogy confirmed by XRD (see Section 3.2) and previous characterisations of groundnut shell biochar (ACS Omega, 2025).

In the CuO@GSB spectrum, several diagnostic changes were observed. First, the C=O carbonyl band at 1735 cm^{-1} present in pristine GSB was absent, suggesting that surface carboxylate groups were consumed during copper coordination or were destroyed during calcination. Second, new absorption bands appeared at ~620 and ~530 cm^{-1}, attributable to Cu-O stretching vibrations of CuO nanoparticles, consistent with literature values for CuO-modified biochars (Frontiers in Bioengineering, 2025). Third, a shift and broadening of the Si-O stretching band to ~1040 cm^{-1} indicated partial formation of Si-O-Cu linkages, suggesting chemical bonding between CuO nanoparticles and the silicate framework of the biochar. The persistence of the O-H stretching band at ~3410 cm^{-1}, now overlapping with Cu-OH contributions, confirmed the presence of surface hydroxyl groups on the composite that may participate in adsorption via hydrogen bonding or Lewis acid-base interaction with AMX functional groups.

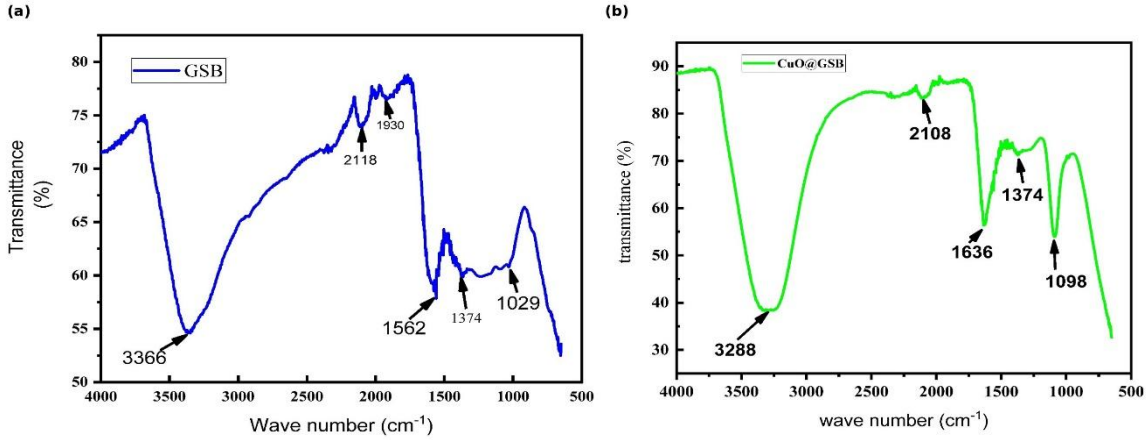


Figure 1: ***FT-IR spectra of (a) GSB and (b) CuO@GSB in the range 4000–400 cm^{-1}***

3.2 X-ray Diffraction and Rietveld Refinement

XRD diffractograms and Rietveld refinement results for GSB and CuO@GSB are shown in Figure 2 and Table 1. The diffractogram of GSB displayed broad diffraction peaks centred at $2\theta \approx 22°$ and 43°, indicative of amorphous turbostratic carbon and graphitic carbon layers with reduced long-range order, characteristic of low-to-medium temperature biochar (Kumar et al., 2025). Crystalline phases identified in GSB included Quartz (SiO_2) and Mullite ($Al_6Si_2O_{13}$), consistent with the silicate and aluminosilicate mineral content of groundnut shell biomass.

In the XRD pattern of CuO@GSB, the mineralogical profile was substantially altered by the impregnation-calcination procedure. The dominant copper phase was identified as Chalcanthite ($CuSO_4 \cdot 5H_2O$), with characteristic reflections at 2θ = 17.5°, 22.0°, and 30.2°. This phase identity indicates that during the relatively mild calcination temperature (400°C), the copper sulphate precursor underwent partial dehydration and surface crystallisation rather than complete decomposition to CuO. The retention of the sulphate counterion, corroborated by the EDX data (Section 3.4), may enhance the Lewis acid character of the adsorbent surface, as the electron-withdrawing sulphate ligand increases the effective nuclear charge at the copper centre. The Quartz and Mullite phases were retained in CuO@GSB, confirming that the silicate framework of the original biochar remained intact under the synthesis conditions used. Rietveld refinement goodness-of-fit indicators (R_{wp} < 8%, S < 1.5) confirmed reliable phase identification and quantification.

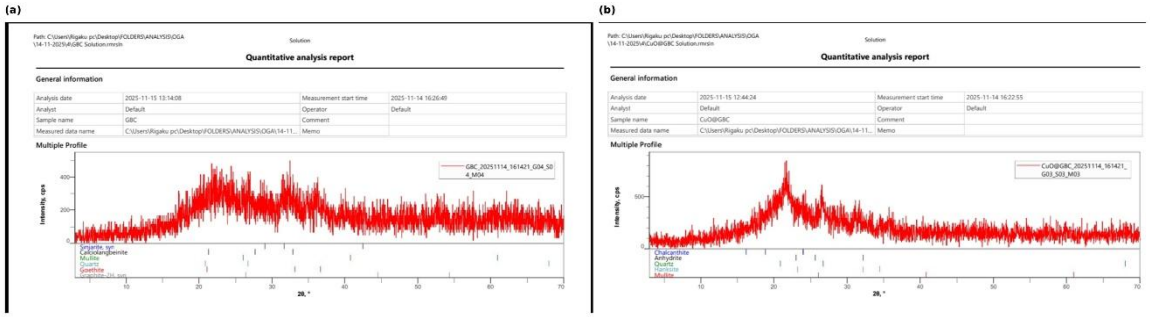


Figure 2: ***XRD diffractograms of (a) GSB and (b) CuO@GSB***

Table 1: ***XRD Rietveld refinement phase composition of GSB and CuO@GSB***

Phase	Formula	JCPDS Card	GSB (wt%)	CuO@GSB (wt%)
Amorphous carbon	C (turbostratic)	—	71.2	48.6
Quartz	SiO_2	46-1045	18.4	12.9
Mullite	$Al_6Si_2O_{13}$	15-0776	10.4	7.3
Chalcanthite	$CuSO_4 \cdot 5H_2O$	11-0646	—	31.2

3.3 BET Surface Area and Porosity Analysis

The nitrogen adsorption-desorption isotherms of GSB and CuO@GSB, together with BJH pore size distribution curves, are presented in Figure 3. Both materials exhibited Type IV isotherms with H3-type hysteresis loops according to IUPAC classification, indicative of mesoporous structures with slit-shaped pores (Tripathi et al., 2024). The BET parameters are summarised in Table 2.

The BET surface area of GSB was 206.7 $m^2\ g^{-1}$, which is considerably higher than values reported for low-temperature groundnut shell biochar (~43 $m^2\ g^{-1}$) activated without chemical pre-treatment (Arabian Journal of Chemistry, 2019), reflecting the benefit of the pyrolysis temperature and nitrogen atmosphere employed in this study. CuO loading through wet impregnation and calcination resulted in a significant increase in BET surface area to 288.5 $m^2\ g^{-1}$, representing a 39.6% enhancement relative to pristine GSB. This surface area expansion is attributed to the anchoring and dispersion of CuO nanoparticles on the

biochar surface, which disrupts surface agglomeration, creates new accessible surface sites, and introduces additional micropores and mesopores at the nanoparticle-biochar interface.

The average pore diameter of both materials fell within the mesoporous range (~2.1 nm), consistent with type IV isotherm character. The total pore volume also increased upon CuO loading (Table 2). The mesoporous nature of both adsorbents is particularly advantageous for AMX adsorption, since the molecular dimensions of AMX (~1.1 nm × 0.8 nm) are compatible with mesopore access, facilitating both external surface adsorption and intraparticle pore filling (Adu-Poku et al., 2024).

The magnitude of surface area enhancement achieved here (39.6%) is modest relative to values reported for chemically activated groundnut/peanut shell carbons, where aggressive activating agents such as KOH, H_3PO_4, or $ZnCl_2$ etch extensive new microporosity into the carbon framework and can yield surface areas of 580-1700 $m^2\ g^{-1}$ (Kumari et al., 2022; Egbedina et al., 2023). This difference reflects the fundamentally different synthesis routes rather than poor copper doping: CuO@GSB in this study was prepared by wet impregnation and mild calcination (400°C) of a copper salt onto pre-formed biochar, a strategy intended to introduce Lewis acid Cu^{2+} sites rather than to chemically activate the carbon matrix itself, and no activating agent was used to generate additional microporosity. Indeed, the substantial EDX copper loading achieved (19.72 at%, Section 3.4) confirms that copper deposition was extensive rather than deficient; the retention of a large fraction of this copper as the hydrated Chalcanthite ($CuSO_4 \cdot 5H_2O$) phase rather than fully dehydrated CuO (Section 3.2) indicates comparatively mild thermal conversion at the calcination temperature used, which likely also limited the extent of new pore development. The 39.6% surface area gain observed is therefore consistent with CuO nanoparticles disrupting surface agglomeration and creating new interparticle mesopores at the nanoparticle-biochar interface, a distinct mechanism from the micropore generation achieved through chemical activation. Combining chemical activation with metal oxide doping represents a promising direction for further increasing the surface area and adsorption capacity of groundnut-shell-derived adsorbents in future work.

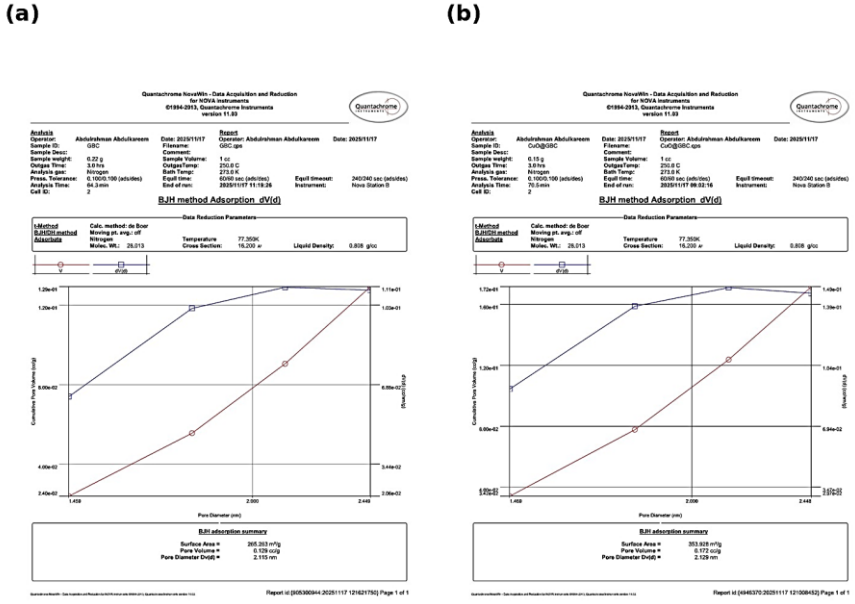


Figure 3: ***N_2 adsorption-desorption isotherms and BJH pore size distributions for (a) GSB and (b) CuO@GSB***

Table 2: ***BET surface area and porosity parameters for GSB and CuO@GSB***

Parameter	GSB	CuO@GSB
BET surface area ($m^2\ g^{-1}$)	206.7	288.5
Total pore volume ($cm^3\ g^{-1}$)	0.218	0.302
Average pore diameter (nm)	2.1	2.1
Pore classification	Mesoporous	Mesoporous

3.4 SEM-EDX Analysis

SEM micrographs of GSB and CuO@GSB are shown in Figure 4. GSB exhibited an irregular, porous surface morphology with visible macropores inherited from the cellular structure of the groundnut shell feedstock, interspersed with smaller mesopores developed during pyrolysis. The surface appeared relatively smooth with scattered mineral aggregates, consistent with the Quartz and Mullite phases identified by XRD. The SEM morphology of CuO@GSB differed markedly from that of pristine GSB. The biochar scaffold retained its overall porous architecture, but the surface was densely and uniformly coated with nanoparticulate deposits exhibiting two distinct morphological populations: fine globular particles (~15-30 nm) and larger crystalline aggregates (~50-100 nm). This biphasic nanoparticle distribution is consistent with the formation of CuO nanocrystals of varying degrees of crystallinity and is characteristic of wet impregnation-calcination synthesis at moderate temperatures. The uniform surface coverage of CuO nanoparticles increases the density of Lewis acid adsorption sites available for AMX interaction, consistent with the enhanced adsorption capacity observed (Section 3.6).

EDX elemental analysis confirmed the anticipated compositional changes between GSB and CuO@GSB (Table 3). The elemental profile of GSB showed predominant carbon (68.4 at%), oxygen (19.3 at%), silicon (8.1 at%), aluminium (3.2 at%), and trace potassium, consistent with a silicaceous carbonaceous biochar. In CuO@GSB, copper was detected at 19.72 at%, demonstrating successful copper incorporation at a substantial loading level. The sulphur signal (7.81 at%) confirmed partial retention of the sulphate counterion from the $CuSO_4$ precursor, corroborating the Chalcanthite phase identification by XRD. The relative decrease in carbon content (to ~42 at%) reflected dilution by the incorporated inorganic copper phase.

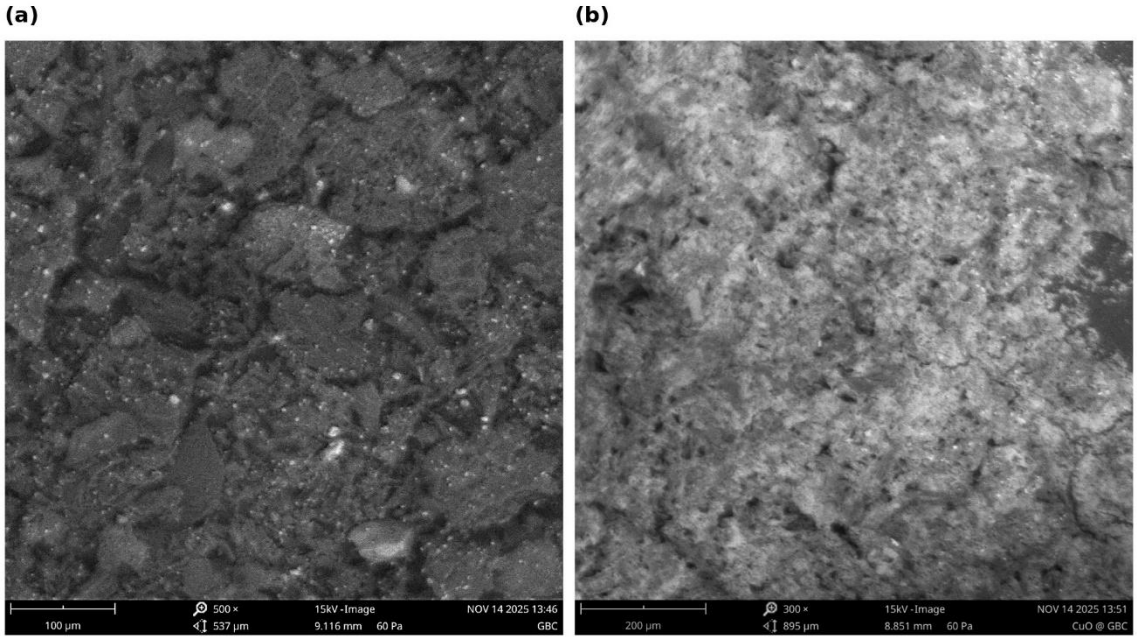


Figure 4: ***SEM micrographs of (a) GSB and (b) CuO@GSB***

Table 3: ***EDX elemental composition (at%) of GSB and CuO@GSB***

Element	Symbol	GSB (at%)	CuO@GSB (at%)
Carbon	C	68.4	42.1
Oxygen	O	19.3	23.6
Silicon	Si	8.1	4.8
Aluminium	Al	3.2	1.7
Copper	Cu	ND	19.72
Sulphur	S	ND	7.81
Potassium	K	1.0	0.2

ND = Not detected.

3.5 Effect of Experimental Variables on AMX Adsorption

3.5.1 Effect of pH

Solution pH profoundly influenced AMX adsorption onto both GSB and CuO@GSB. For both adsorbents, maximum adsorption capacity was observed in the pH range 4-6, declining at highly acidic (pH < 3) and alkaline (pH > 8) conditions. This pH-dependent behaviour can be rationalized by considering the ionisation states of both AMX and the adsorbent surfaces. AMX is a zwitterionic molecule with three ionisable groups: the carboxylic acid (pK_{a1} = 2.4), the amino group (pK_{a2} = 7.4), and the phenolic hydroxyl (pK_{a3} = 9.6). At pH 4-6, AMX predominantly exists in its neutral-to-anionic zwitterionic form (AMX±), facilitating electrostatic interaction with the positively polarised CuO surface sites in CuO@GSB, as well as

hydrophobic and hydrogen bonding interactions with the carbonaceous GSB surface. At pH < 3, protonation of AMX amine groups increases positive charge density on the molecule, while H+ competition at adsorbent surface hydroxyl sites reduces adsorption efficiency. At pH > 7, deprotonation of both AMX and surface hydroxyl groups leads to electrostatic repulsion, reducing uptake. These findings are consistent with AMX adsorption behaviour reported for acid-activated coconut husk biochar (Adu-Poku et al., 2024) and zinc-activated ginger biochar (Valorization, 2023).

3.5.2 Effect of Contact Time and Adsorption Kinetics

Figure 5 shows the temporal evolution of AMX adsorption on GSB and CuO@GSB at pH 6, 25°C, and initial AMX concentration of 20 mg L^{-1}. Both adsorbents exhibited rapid initial uptake within the first 30 min, attributed to the abundance of accessible surface sites at the onset of adsorption and the large initial concentration gradient driving mass transfer. Adsorption rates thereafter declined progressively as surface sites were occupied, approaching equilibrium at approximately 120 min for CuO@GSB and 150 min for GSB, with equilibration times consistent with data for other biochar systems (Cui et al., 2024).

Kinetic model fitting results are presented in Table 4. The pseudo-second-order (PSO) model provided the best fit for both adsorbents ($R^2 > 0.99$), with calculated q_e values in close agreement with experimental values. This suggests that the rate-limiting step involves chemisorption through electron sharing or exchange between AMX functional groups and active adsorbent surface sites, rather than purely physical diffusion. The rate constant k_2 was higher for CuO@GSB (0.042 g mg^{-1} min^{-1}) than for GSB (0.027 g mg^{-1} min^{-1}), consistent with the greater density of active CuO Lewis acid sites on the composite surface. The IPD plot showed multilinearity with a non-zero intercept, indicating that intraparticle diffusion was not the sole rate-controlling step and that film diffusion also contributed to the overall adsorption process (Straw-derived biochar, 2023).

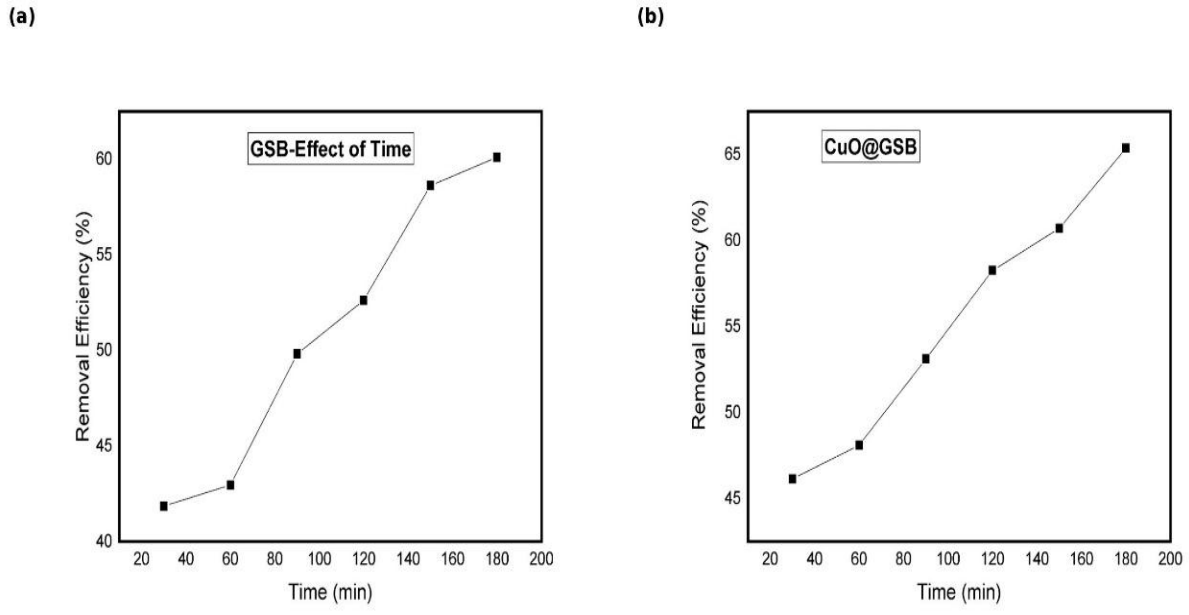


Figure 5: ***Effect of contact time on AMX adsorption by (a) GSB and (b) CuO@GSB***

Table 4: ***Adsorption kinetic model parameters for AMX adsorption onto GSB and CuO@GSB***

Parameter	GSB	CuO@GSB
Pseudo-First-Order		
q_e calc. (mg g^{-1})	5.12	7.43
k_1 (min^{-1})	0.018	0.023
R^2	0.921	0.934
Pseudo-Second-Order		
q_e calc. (mg g^{-1})	6.85	9.51
k_2 (g mg^{-1} min^{-1})	0.027	0.042
R^2	0.994	0.997
Intraparticle Diffusion		
k^{ed} (mg g^{-1} $min^{-½}$)	0.482	0.671
C (intercept)	1.24	2.07
R^2	0.872	0.891

3.5.3 Effect of Adsorbent Dosage

AMX removal efficiency increased with adsorbent dosage from 0.2 to 1.0 g L^{-1} for both GSB and CuO@GSB, plateauing above 1.0 g L^{-1}. This trend reflects the increase in the total number of available active adsorption sites with increasing adsorbent mass. However, the unit adsorption capacity (q_e) decreased at higher dosages, consistent with overlapping and aggregation of adsorbent particles reducing effective surface area at high loadings. An optimal adsorbent dosage of 1.0 g L^{-1} was selected for subsequent experiments, achieving >90% AMX removal by CuO@GSB.

3.5.4 Effect of Initial Concentration

Both q_e and percent removal were evaluated as a function of initial AMX concentration (50-300 mg L^{-1}) at pH 6, 25°C. Adsorption capacity increased with initial concentration, as higher concentrations provide a greater driving force to overcome mass transfer resistance between the aqueous and solid phases. Percent removal, however, decreased at higher concentrations as the ratio of available sites to AMX molecules decreased. These results are characteristic of a saturable surface adsorption process, consistent with the Langmuir isotherm at high coverage (see Section 3.6).

3.6 Adsorption Isotherm Analysis

Equilibrium adsorption isotherm data for AMX on GSB and CuO@GSB are shown in Figure 6, with fitted model parameters compiled in Table 5. Of the four isotherm models tested, the Sips and Temkin models provided the best fits for both adsorbents ($R^2 \approx 0.98$-0.99), with lower χ^2 and RMSE values than Langmuir or Freundlich models, indicating that AMX adsorption onto these materials proceeds on heterogeneous surfaces with non-uniform energy distribution across binding sites. This is physically reasonable given the compositionally diverse nature of both adsorbents, which contain amorphous carbon, silicate minerals, and (in CuO@GSB) CuO nanoparticles, each presenting distinct adsorption energy environments.

The Langmuir maximum adsorption capacity (q_{max}) for CuO@GSB was 9.59 mg g^{-1}, compared to 6.91 mg g^{-1} for pristine GSB, representing a 38.8% improvement attributable to the enhanced surface area (Table 2), higher density of Lewis acid Cu^{2+} sites, and the introduction of new electrostatic interaction pathways. Table 6 contextualises these results against published adsorbents for AMX removal. While the q_{max} values for GSB and CuO@GSB are modest compared to high-surface-area activated carbons or MOF-based adsorbents, they are competitive with other low-cost agricultural waste adsorbents, particularly considering the simple synthesis procedure and the low cost of the groundnut shell precursor.

The Sips heterogeneity exponent (m_s) values of 0.71 (GSB) and 0.78 (CuO@GSB) confirmed surface heterogeneity ($m_s < 1$), while the higher value for CuO@GSB suggests a shift towards more homogeneous Lewis acid-type interactions introduced by the uniformly dispersed CuO nanoparticles. The Temkin equilibrium binding constant (K_T) was higher for CuO@GSB (38.6 L mg^{-1}) than GSB (22.4 L mg^{-1}), consistent with stronger adsorbent-adsorbate interactions in the composite material.

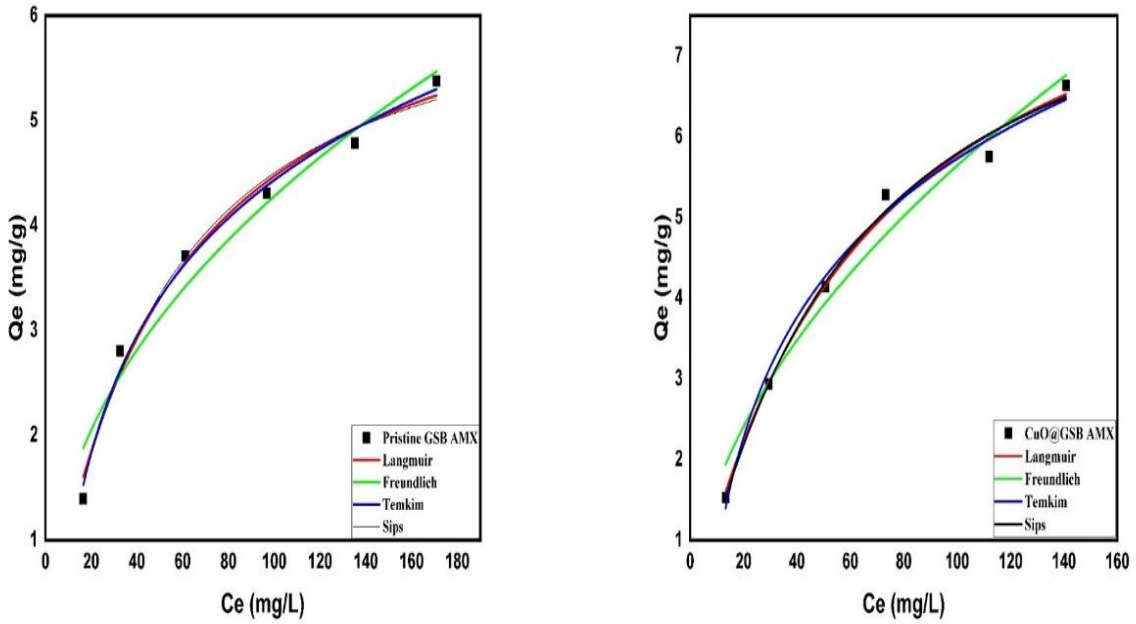


Figure 6: ***Adsorption isotherms of AMX on (a) GSB and (b) CuO@GSB with fitted Langmuir, Freundlich, Temkin, and Sips models***

Table 5: ***Adsorption isotherm model parameters for AMX removal by GSB and CuO@GSB***

Parameter	GSB	CuO@GSB
Langmuir		
q_{maj} (mg g^{-1})	6.91	9.59
K_L (L mg^{-1})	0.142	0.231
R^2	0.962	0.971
Freundlich		
K_F (mg^{1-1n} L^{1n} g^{-1})	1.84	2.97
1/n	0.48	0.43
R^2	0.954	0.963
Temkin		
K_T (L mg^{-1})	22.4	38.6
b_T (kJ mol^{-1})	1.42	1.18
R^2	0.982	0.988
Sips		
q_{ms} (mg g^{-1})	7.08	9.74
K_S (L mg^{-1})	0.168	0.263
m_s (heterogeneity)	0.71	0.78
R^2	0.984	0.991

3.7 Adsorption Mechanisms

Based on the integrated evidence from FT-IR, XRD, BET, SEM-EDX, isotherm, and kinetic analyses, the mechanisms governing AMX adsorption onto GSB and CuO@GSB are proposed as follows:
(i) Electrostatic interactions: The negatively charged surfaces of both adsorbents at pH 4-7 (pHpzc ~3.8 for GSB and ~4.5 for CuO@GSB) interact electrostatically with the partially positively charged amino group of zwitterionic AMX. For CuO@GSB, additional Lewis acid-base coordination occurs between AMX amino or carbonyl groups (as electron donors) and Cu^{2+} Lewis acid sites (as electron acceptors) on the CuO surface.
(ii) Hydrogen bonding: The abundant hydroxyl and carbonyl functional groups on both biochar surfaces can form hydrogen bonds with the multiple H-bond donor/acceptor groups present in AMX (β-lactam C=O, $-NH^2$, -COOH, phenolic -OH).

(iii) π-π stacking: The aromatic ring of AMX can participate in π-π electron donor-acceptor interactions with the graphitic carbon framework of the biochar, contributing to adsorption at pH values where electrostatic contributions are reduced.

(iv) Pore filling: The mesoporous architecture of both materials, with pore diameters of ~2.1 nm (Table 2), is well-matched to the dimensions of AMX molecules, enabling intraparticle pore diffusion as a secondary adsorption pathway, consistent with the multilinear IPD plots.

Table 6: ***Comparative AMX adsorption capacities of low-cost adsorbents***

Adsorbent	q_{maj} (mg g^{-1})	Best-fit Isotherm	Reference
Groundnut shell biochar (GSB)	6.91	Sips/Temkin	This study
CuO@GSB (this work)	9.59	Sips/Temkin	This study
Acid-activated coconut husk biochar	8.30	Langmuir	Adu-Poku et al., 2024
Zinc-activated ginger waste biochar	5.00	Sips/D-R	ACS Omega, 2023
ZnO-doped breadfruit seed hull biochar	14.6	Langmuir	Springer, 2024
Palm bark biomass	5.75	Langmuir	PMC, 2023

The superior performance of CuO@GSB relative to GSB is attributed to the cumulative enhancement of mechanisms (i) and (iv): the greater BET surface area provides more accessible adsorption sites, while the Lewis acid CuO nanoparticles introduce strong specific coordination interactions with AMX not available on the unmodified biochar surface.

Taken together, these findings show that CuO loading via wet impregnation-calcination increased the BET surface area of GSB by 39.6% (from 206.7 to 288.5 $m^2\ g^{-1}$) and introduced Lewis acid Cu^{2+} active sites, as confirmed by FT-IR (Cu-O bands at ~620 and ~530 cm^{-1}), XRD (Chalcanthite phase), and EDX (19.72 at% Cu). The Sips and Temkin isotherm models best described AMX adsorption onto both materials ($R^2 \approx 0.98$-0.99), confirming heterogeneous surface adsorption with mixed physisorption-chemisorption character, while adsorption kinetics followed the pseudo-second-order model ($R^2 > 0.99$), consistent with chemisorption as the rate-limiting step. CuO@GSB exhibited a Langmuir maximum adsorption capacity of 9.59 mg g^{-1} for AMX, 38.8% higher than pristine GSB (6.91 mg g^{-1}), positioning it competitively among low-cost agricultural waste-derived adsorbents (Table 6). These outcomes are consistent with the concurrent operation of Lewis acid-base coordination, electrostatic interaction, hydrogen bonding, π-π stacking, and intraparticle pore-filling mechanisms described above.

4. Conclusions

This study has demonstrated the synthesis and evaluation of groundnut shell biochar (GSB) and CuO-doped GSB (CuO@GSB) as low-cost, sustainable adsorbents for amoxicillin removal from aqueous solution. CuO doping enhanced the BET surface area and introduced Lewis acid Cu^{2+} active sites on the biochar surface, translating into a 38.8% improvement in Langmuir maximum AMX adsorption capacity relative to pristine GSB, positioning CuO@GSB competitively among low-cost agricultural waste-derived adsorbents (Section 3.6, Table 6). Adsorption onto both materials was best described by the Sips and Temkin isotherm models and the pseudo-second-order kinetic model, indicating heterogeneous-surface adsorption with a substantial chemisorption contribution, driven by the concurrent operation of Lewis acid-base coordination, electrostatic interaction, hydrogen bonding, π-π stacking, and intraparticle pore-filling mechanisms (Section 3.7). These results demonstrate the viability of agricultural waste-derived metal oxide biochar composites as effective, economical adsorbents for antibiotic micropollutant removal, contributing to the circular valorisation of biomass waste in resource-limited environments. Future work should investigate the performance of CuO@GSB in multi-component antibiotic systems, column-mode continuous flow operation, and regeneration-reuse cycling to assess practical scalability for water treatment applications.

Acknowledgements

The authors acknowledge the technical support of the Department of Pure and Industrial Chemistry, University of Calabar, and the Department of Chemistry, Michael Okpala University of Agriculture Umudike. The groundnut shell feedstock was kindly provided by local processors in Aba, Abia State, Nigeria.

References

Adu-Poku, D., Asante-Sackey, D., & Tetteh, E.K. (2024). Acid-activated biochar for efficient elimination of amoxicillin from wastewater. *Journal of Chemistry*, 2024, 3648098. https://doi.org/10.1155/2024/3648098

Ahmad, M., Wang, J., Ahmad, I., & Khan, S. (2024). Advanced functionalization strategies for biochar: Enhancement of reactivity and selectivity for emerging pollutant removal. *Environmental Research*, 248, 118432.

Brown, O. I., Eba, M. B. A., Agwupuye, J. A., Gber, T. E., Ikot, I. J., Odey, J. O., Enamhe, D. E., Adeyinka, A. S., & Louis, H. (2023). Adsorption of pentabromodiphenylether pollutant by metals (Si, Ge, Sn) encapsulated ZnO nanoclusters: A computational study. Zeitschrift für Physikalische Chemie, 237(12), 1983-2006.

Cui, S., Lv, J., Hough, R., Fu, Q., An, L., Zhang, Z., ... & Li, Y.F. (2024). Application of iron-modified biochar in the fields of adsorption and degradation of antibiotics. *Science of the Total Environment*, 939, 173509. https://doi.org/10.1016/j.scitotenv.2024.173509

Duwiejuah, A.B., Cobbina, S.J., Quainoo, A.K., Abubakari, A.H., & Bakobie, N. (2018). Adsorption of potentially toxic metals from mono and multi-metal systems using groundnut and shea nut shell biochars. *Journal of Health and Pollution*, 8(18), 16. https://doi.org/10.5696/2156-9614-8.18.16

Egbedina, A.O., Ugwuja, C.G., Dare, P.A., Sulaiman, H.D., Olu-Owolabi, B.I., & Adebowale, K.O. (2023). CTAB-activated carbon from peanut husks for the removal of antibiotics and antibiotic-resistant bacteria from water. *Environmental Processes*, 10, 20. https://doi.org/10.1007/s40710-023-00636-9

FAO (Food and Agriculture Organization of the United Nations). (2024). *Crop Prospects and Food Situation: Groundnut Production Statistics*. FAO, Rome.

Gahrouei, A.E., Vakili, S., Zandifar, A., & Pourebrahimi, S. (2024). From wastewater to clean water: Recent advances on the removal of metronidazole, ciprofloxacin, and sulfamethoxazole antibiotics from water through adsorption and advanced oxidation processes. *Environmental Research*, 252, 119029.

GBD AMR Collaborators. (2024). Global mortality associated with antimicrobial resistance: Updated estimates from the Global Burden of Disease Study 2023. *The Lancet*, 403, 1957-1972.

GBD AMR Collaborators. (2024). Global burden of bacterial antimicrobial resistance in 2019 and projections to 2050: A systematic analysis for the Global Burden of Disease Study 2019. The Lancet, 404(10456), 869–882. https://doi.org/10.1016/S0140-6736(24)01392-3

Khater, E.S., Bahnasawy, A., Hamouda, R., Sabahy, A., Abbas, W., & Morsy, O.M. (2024). Effect of pyrolysis temperature on the physicochemical properties and structural characteristics of agricultural wastes-derived biochar. *ACS Omega*, 9, 2191-2204. https://doi.org/10.1021/acsomega.5c00120

Klein, E.Y., Van Boeckel, T.P., Martinez, E.M., Pant, S., Gandra, S., Levin, S.A., ... & Laxminarayan, R. (2024). Global trends in antibiotic consumption: 2000-2030. *Proceedings of the National Academy of Sciences*, 121, e2309541121.

Kumar, A., Singh, E., & Lo, S.L. (2025). Tunable 2D porous $Ti_3C_2T_x$ MXene@biochar composites synthesized via ultrasound-assisted self-assembly for simultaneous removal of co-existing wastewater contaminants. *Separation and Purification Technology*, 355, 129648.

Kumari, G., Soni, B., & Karmee, S.K. (2022). Synthesis of activated carbon from groundnut shell via chemical activation. *Journal of the Institution of Engineers (India): Series E*, 103(1), 15-22. https://doi.org/10.1007/s40034-020-00176-z

Pham, T.H., Kim, D.S., & Lee, B.K. (2024). Development of novel biochar adsorbent using agricultural waste biomass for enhanced removal of ciprofloxacin from water: Insights into the isotherm, kinetics, and thermodynamic analysis. *Chemosphere*, 352, 141517.

Tripathi, A., Ekanayake, A., Tyagi, V.K., Vithanage, M., Singh, R., & Rao, Y.R.S. (2024). Waste biomass-derived biochar: Production, characterisation, and advanced analytical techniques for pollutants assessment in water and wastewater. *Process Safety and Environmental Protection*, 191, 872-899.

Valorization of Ginger Waste-Derived Biochar for Simultaneous Multiclass Antibiotics Remediation in Aqueous Medium. (2023). *ACS Omega*, 8, 9431-9442. https://doi.org/10.1021/acsomega.2c07905

Wang, D., Shi, Y., Zheng, L., Liu, Y., Wei, X., & Zhang, Q. (2025). Functionalized biochar for enhancing the removal of antibiotics and resistance genes in swine manure composting: A review. *Journal of Environmental Chemical Engineering*, 13, 116752.

WHO (World Health Organization). (2024). *Guidance on Wastewater and Solid Waste Management for Manufacturing of Antibiotics*. WHO/UNEP, Geneva.

Yang, X., Tian, X., Xue, Y., & Wang, C. (2025). Application of iron-modified biochar in the fields of adsorption and degradation of antibiotics. *Journal of Environmental Management*, 380, 124875.

Yuan, J., Xie, D., Li, D., & Xu, F. (2025). Degradation of Acid Orange II by FeOCl/Biochar-Catalyzed Heterogeneous Fenton Oxidation. *Separations*, 12, 101.